

High-Energy-Density Graphene Hybrid Flexible Fiber Supercapacitors

Yifan Zhou,^[a] Fanglan Guan,^{*[a]} Fangfei Zhao,^[a] Yangmiao Shen,^[a] and Lihong Bao^[a]

Graphene fiber-based supercapacitors (GFSCs) as flexible energy-storage devices have achieved much in the wearable electronics. However, the GFSCs still suffer insufficient energy density, and of which desirable balance between mechanical and electrochemical properties has not been realized. Herein, we developed AgI and conductive polymer assisted co-enhancement strategy to prepare the high-performance GFSCs with super-high energy density, favorable mechanical properties, and superior electrochemical properties. The conductive binder polymer, poly(3,4-ethylenedioxythiophene) (PEDOT) was introduced into the GO spinning solution to enhance RGO fiber strength, conductivity, and electrochemical performance by

forming a strong interface with GO in the spinning solution. On the other hand, the synergistic effect of micro- and nano-scale AgI grown on the fiber surface and aqueous gel electrolyte widen the potential window of the GFSC to 1.6 V, which is much higher than that of reported GFSCs, and resulting in a significantly increased energy density. At 0.1 A cm⁻³, the volumetric capacitance and energy density of the fabricated GFSCs are as high as 166.6 F cm⁻³ and 29.65 mWh cm⁻³, respectively. The high strength and flexibility of the hybrid fibers endowed the GFSCs with ~100% capacitance retention when bent to 180°. This work opens a new way to design and fabricate high-performance GFSCs.

Introduction

Electronic smart textiles show many new possibilities and great application potential in different fields for consumer groups because of their unique natures such as light weight, flexibility and high integration. In order to build a whole electronic textile system, all kinds of flexible electronic devices such as fiber transistors,^[1] fiber OLEDs^[2] and fiber energy devices^[3] have been developed to integrate with textile. Among these, 1D electronic functional fiber with their easily handling characteristics and excellent weaving into 2D textile has become the focus issue which many novel fabrication approaches have been developed.

Because of the high electrical performance, good stability, resisting stretching, bending, twisting deformations and easy to assemble into wearable electronics, graphene-based fiber-shaped supercapacitors (GFSCs) as flexible energy storage devices were intensively studied and also great advances have been made.^[4–6] However, the low power density and energy density hindered them from being used in e-textile.^[7–9] Many works have been executed to improve their specific capacitance by adding pseudocapacitive active materials into the graphene oxide (GO) spinning solution.^[10–13] An asymmetric fiber-based supercapacitors (FSCs) configuration and ionic liquid electrolytes have also been developed to widen the operating voltage window.^[14–16] Zhang et al. made a highly-conductive Ti₃C₂T_x MXene hybrid PEDOT fiber, but the fiber was

too weak to be weaved into 2D textile.^[17] Qu et al. prepared hollow graphene/PEDOT polymer fibers with strong mechanical properties that could be processed with other industrial fibers. The volumetric energy density of it was just on-par with that of 4 V-500 μAh thin-film lithium.^[18] Many fiber supercapacitors have been developed with a high energy density and desirable mechanical properties.^[19]

Although great progress has been made for GFSCs, great challenges still exist for fiber supercapacitors such as insufficient mechanical properties, low energy density, and the low efficiency of the gel electrolyte.^[20–22] For most GFSCs, the potential windows mainly in the 1 V range, researchers always broaden the potential windows to improve the energy density through series or parallel connection of multi-fiber supercapacitors because the energy density was directly proportional to the square of the potential window and specific capacitance.^[23] However, the potential window of GFSCs using PVA/H₂SO₄ gel-electrolyte was limited to 1 V which also restricted the specific capacitance improvement of GFSCs. Thus, it is still a big challenge to improve the energy density of GFSCs only through increasing the specific surface area of the electrode material such as porous graphene^[24] and hybrid graphene.^[25] Wang et al. prepared high-energy-density RuO₂-loaded PEDOT fibers whose voltage window reaches 1.6 V while the fiber strengthen was only 123 MPa, which was extremely difficult to be weaved into 2D textile.^[26]

Although great progresses have been made for the capacitance and energy density of the GFSCs, they still cannot reconcile the numerous properties including energy density, strength, light weight and safety for practical applications in e-textiles. Generally, transition metal oxides and conductive polymers are used to improve the electrochemical performance, but the poor interfacial properties between graphene oxide sheets and other hybrid components often affect the

[a] Y. Zhou, Prof. F. Guan, F. Zhao, Y. Shen, Prof. L. Bao
School of Materials Design and Engineering
Beijing Institute of Fashion Technology
Beijing 100029 (P. R. China)
E-mail: clygl@bjft.edu.cn

 Supporting information for this article is available on the WWW under
<https://doi.org/10.1002/batt.202200536>

mechanical properties of graphene fibers. Studies have shown that certain bonds can be formed between PEDOT and GO, which are also helpful to the fiber strength through bonding the graphene sheets closely, which gives us a good inspiration to fabricate GFSCs.^[27,28]

In general, liquid electrolytes in supercapacitor caused safety problems and low potential window hindered the development of supercapacitors. In order to deal with this shortcomings, much efforts have been made. AgI was firstly found to possess promising ionic conductivity and polarizability, which can widen the potential window.^[29–31] Much efforts were made to explore AgI and its derivatives in the supercapacitors or batteries field.^[32,33]

The reduction and washing processes of reduced graphene oxide (RGO) fibers produce a large amount of toxic hydroiodic acid waste liquid. Herein, we utilize I⁻ on RGO fibers after reduction to deposit the solid electrolyte AgI on the RGO fiber. This broadens the potential window of RGO FSCs and also reduces the washing step. We design graphene hybrid fiber supercapacitors with high energy storage by loading AgI solid electrolytes onto the fiber surface. PEDOT:PSS, acting as a conductive adhesive, is added to the graphene oxide spinning solution, which provide the PEDOT:PSS/RGO fiber with increased flexibility and electrical conductivity. The optimized PEDOT:PSS composition of 20 wt% improved the fiber strength by 137%. The strength of PEDOT:PSS/RGO fibers loaded with AgI is enhanced by 153%, which gradually make the weaving or processing graphene fiber into 2D textile possible. The potential window of a single AgI/PEDOT:PSS(20%)/RGO(80%) fiber supercapacitors (PG3-AgI FSCs) can reach 1.6 V, which has rarely been reported in previous work. At the current density of 0.1 A cm⁻³, the capacitance and the energy density of the fibers is 166.6 F cm⁻³ and 29.65 mWh cm⁻³, respectively. After 5000 cycles, the capacitance retention is 88%. Three PG3-AgI FSCs in series could power two in-series red light emitting diodes (LEDs) for ten minutes. This shows that GFSCs loaded with solid electrolyte and conductive polymer have broad application prospects in portable, flexible, small wearable electronic energy storage. This work points out a new direction for manufacturing high performance of fiber-based supercapacitors with great mechanical behavior and electrochemical performance.

Results and Discussion

Morphology characterization of RGO composite fibers

AgI/PEDOT:PSS/RGO composite fibers were prepared through wet spinning and surface growth (Figure 1a). In short, RGO fibers (Figure 1b) or PEDOT:PSS/RGO fibers (Figure 1d) were prepared by extruding GO spinning solutions containing different mass percentages of PEDOT:PSS into an acetic acid bath and then washing with ethanol and water. PEDOT:PSS blended well with GO even when the mixing ratio of PEDOT:PSS is as high as 50 wt%, forming homogeneous spinning solutions. PG_x fibers, where P, G, and x symbolize PEDOT:PSS, RGO, and PEDOT:PSS contents ($x=1, 2, 3, 4, 5, 6$ and 7 indicate

PEDOT:PSS contents of 10 wt%, 15 wt%, 20 wt%, 25 wt%, 30 wt%, 40 wt% and 50 wt%, respectively). The reduced PEDOT:PSS/RGO fiber without washing off I⁻ was immersed in AgNO₃ ethanol solution to obtain AgI/PEDOT:PSS/RGO fibers (Figure 1f). The yellow and green elemental maps in Figure 1(h) revealed the existence of AgI particles deposited on the fiber surface or inside the fibers (Figure 1f, g). XRD patterns showed that the prepared AgI contained β -AgI crystals (Figure 2c).

The SEM shows that the surface of pure RGO fibers exhibits vertical gully and horizontal wrinkles (Figure 1b) and the cross section inserted in Figure 1(b) was typical layered structure. While the surface of PG3 fiber appears more smoothly (Figure 1d) than that of RGO fiber and a closer lamellar structure in cross section (Figure 1e). This microstructure of PG3 fiber may be due to the bonding between PEDOT and GO in the spinning solution that RGO sheet was finally coated and bonded by PEDOT, so that the composite fiber forms a relatively dense sheets and smooth fiber surface. Due to the coating of short-chain PEDOT, the d-spacing of the PG3 fiber switched to 3.57 Å from 3.67 Å of RGO sheets calculated according to XRD patterns in Figure S1(c) and the orientation degree of the PG3 fiber decreases to 67% from 75% of RGO fiber, as shown in Figure S1(d). Accordingly, the flexibility and strength of the PG3 fibers are all improved, as shown in Figure 3(a). C, O, S, I, and Ag atoms were detected throughout the PG3-AgI fiber (Figure 1h).

Structural features of RGO composite fibers

Structural characteristics of RGO composite fibers were explored using Raman spectroscopy, FTIR, and XRD. Raman and infrared spectra showed that π - π stacking and hydrogen bonding interlayer forces formed between PEDOT and RGO, which give rise to the strength and electrical conductivity of PG3 fiber.

The Raman spectra of PEDOT:PSS/RGO composite fiber exhibited a strong blueshift (Figure 2a). The detection of the D band (1351 cm⁻¹), G band (1586 cm⁻¹), and 2D band (2695 cm⁻¹) of RGO and detection of the signature peaks of PEDOT:PSS (574, 990, 1270, 1430, and 1511 cm⁻¹) in the Raman spectrum of PEDOT:PSS/RGO fibers illustrate the uniform distribution of PEDOT:PSS in RGO composite fibers.^[34–36] In the PEDOT:PSS/RGO fiber, the D+G peaks for RGO were split into multiple peaks, which declared variations in the stacking sequence of the RGO sheets.^[37] The peaks at 1256 cm⁻¹ and 1423 cm⁻¹ in the Raman spectrum of PEDOT:PSS fibers blue-shifted to 1270 cm⁻¹ and 1430 cm⁻¹ in the Raman spectrum of PEDOT:PSS/RGO fibers, respectively. These blue shifts indicate the phase separation between PEDOT and PSS and tight alignment between the graphene-sheet network and PEDOT, which are induced by strong π - π interactions of RGO with PEDOT or PSS.^[38]

The Raman spectrum of PEDOT:PSS/RGO fibers also revealed that PEDOT:PSS conformation changed from benzoid dominant to quinoid dominant. This indicates the dominance of linear or expanded-coil conformation of PEDOT in the fibers,

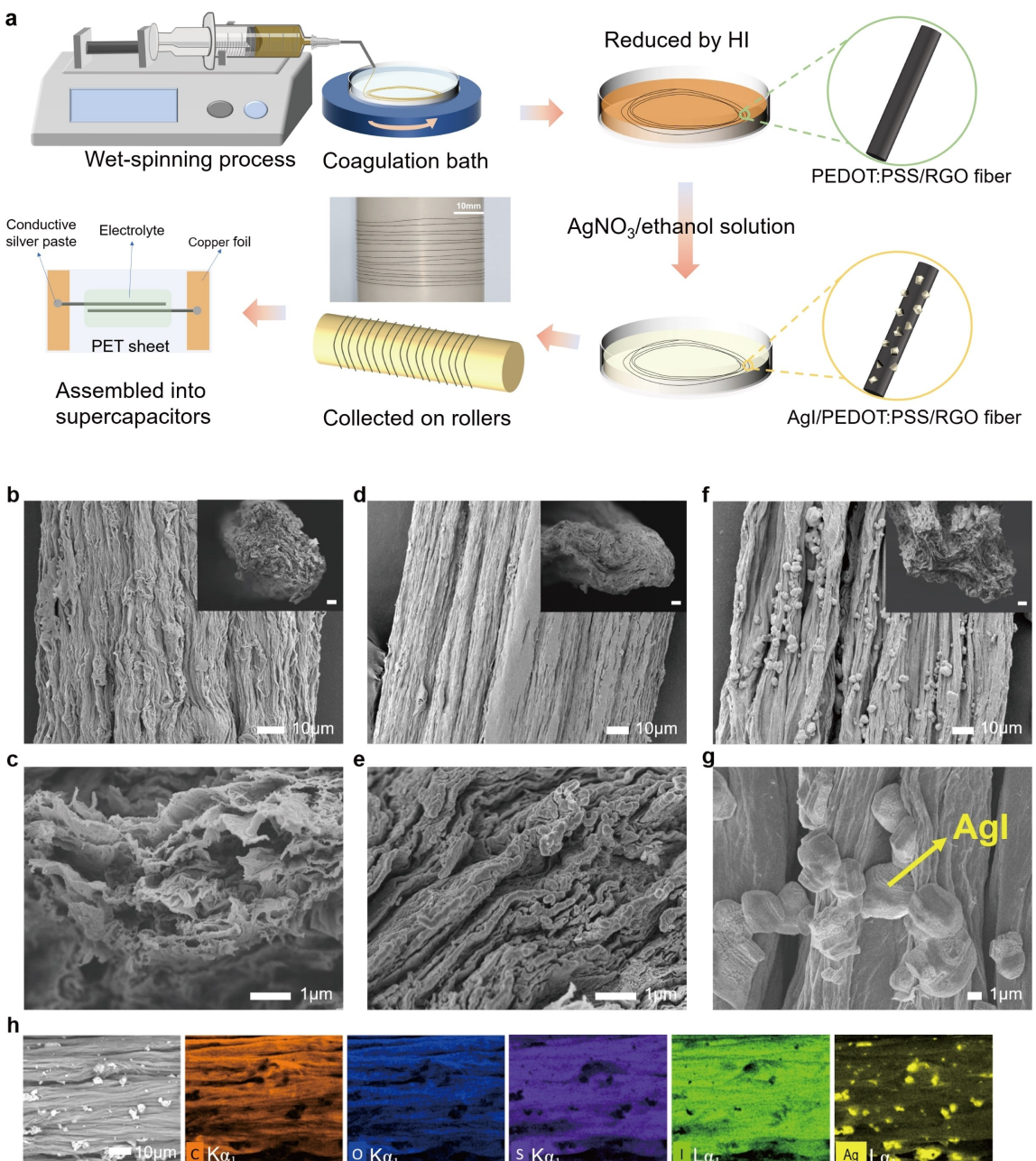


Figure 1. a) The process of fabricating AgI/PEDOT:PSS(20%)/RGO(80%) fibers and digital photograph of the fibers collected on a PTFE cylinder. b) The SEM image of RGO fiber surface (inserted graph is the cross section of RGO fiber). c) The cross sectional SEM image of RGO fiber in a large magnification. d) The SEM image of PEDOT:PSS(20%)/RGO(80%) fiber surface (inserted graph is the cross section of this fiber). e) Magnified view of the cross section SEM image of PEDOT:PSS(20%)/RGO(80%) fiber. f) The SEM image of AgI/PEDOT:PSS (20%)/RGO(80%) fiber surface (inserted graph is the cross section of this fiber). g) The SEM image of AgI/PEDOT:PSS(20%)/RGO(80%) fiber surface in a large magnification. h) Energy Dispersive X-Ray Spectroscopy (EDX) maps of carbon, oxygen, sulfur, iodine, and silver atoms of the sample shown in (g). The size of the scale bars in (b, d, f) are 10 μm.

contributing to the delocalization of π -electrons throughout the PEDOT chains.^[39,40] This conformational change promoted carrier mobility in the PEDOT:PSS/RGO fiber supercapacitor. Furthermore, strong π - π interactions between RGO and PEDOT:PSS promote carrier transport by lowering the carrier-hopping barrier.^[41-43]

The FTIR spectra (Figure 2b) of PEDOT:PSS, RGO, and PGx fibers also validated the conclusions of the Raman spectra. There were peaks connected to the S=O (1060 and 1160 cm⁻¹)

bonds and S-phenyl (1121 cm⁻¹) bond of sulfonic acid, peaks connected to the C=C or C=C bonds (1270, 1533, and 1560 cm⁻¹) of thiophene, and a peak connected to the C=S bonds (712 cm⁻¹) of thiophene in the FTIR spectrum of PEDOT:PSS.^[44] In PEDOT:PSS/RGO fibers with different mixing ratios, the red shift of the –CH₂ asymmetric stretching and CH₂ symmetric stretching peaks from 2920 cm⁻¹ and 2850 cm⁻¹ to 2914 cm⁻¹ and 2846 cm⁻¹ assigned to the PEDOT conformation change leading to the variation of its steric hindrance. As the

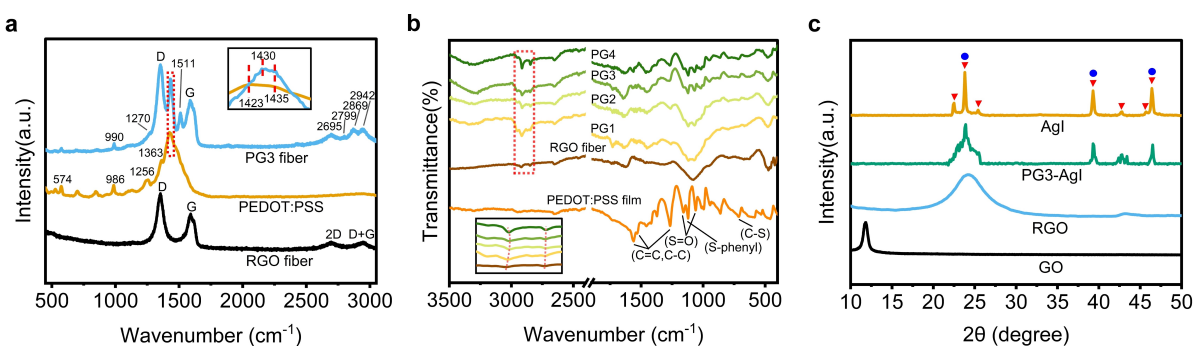


Figure 2. a) The Raman spectra and b) FTIR spectra of RGO fibers, PEDOT:PSS, and PGx fibers. c) The XRD patterns of AgI powder, PG3-AgI fibers, RGO fibers, and GO powder.

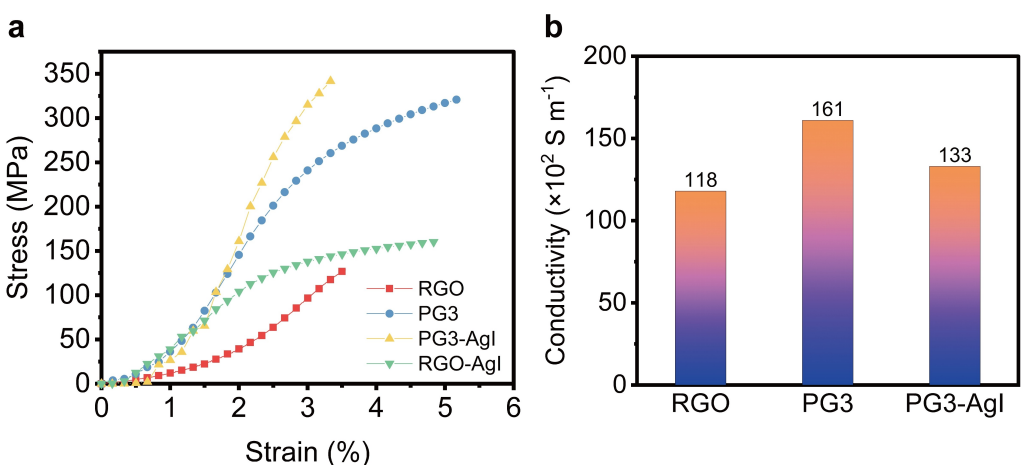


Figure 3. a) The stress-strain curves of RGO, PG3, RGO-Agl, and PG3-Agl fibers. b) Electrical conductivity of RGO, PG3, and PG3-Agl fibers.

amount of PEDOT:PSS in PEDOT:PSS/RGO fibers increased, the peak at 3300 cm^{-1} , which represents hydrogen bonding, became wider. This indicates that many hydrogen bonds formed between RGO and PEDOT:PSS molecules. Raman and FTIR measurement spectra both indicated that PEDOT:PSS formed strong $\pi-\pi$ interactions and hydrogen bonds with RGO sheets, which were reflected in the PEDOT:PSS/RGO composite fiber tensile strength.

XRD analysis was employed to investigate the crystal structure of the solid electrolyte AgI. The scattering peaks of PG3-Agl fibers (Figure 2c) were sharp and showed peaks for AgI solid powder and RGO sheets. The sharp peaks at 23.9° , 39.3° , and 46.5° were related to the three planes ((002), (110), and (112), respectively) of β -phase AgI (red triangles) and/or three planes ((111), (220), and (311), respectively) of γ -phase AgI (blue circles). This indicated successful growth of AgI onto PEDOT:PSS/RGO fibers.

Mechanical and electrical properties

Figure 3(a and b) displays the stress-strain curves and electrical conductivity of RGO, PG3 and PG3-Agl fibers respectively. The

stress-strain curves and electrical conductivity of other formulated samples were illustrated in Figures S2 and S3.

It was obvious that strengthen and toughen effects of conductive bonding PEDOT on RGO fibers reached the highest at PEDOT 20 wt% content which could be ascribed to the intrinsic conductivity of PEDOT and good interface effect forming between PEDOT and GO. More than 20 wt% PEDOT in spinning solution would influence the process of fiber formation which directly led to the decrease of fiber strength. Too much PEDOT accumulates between RGO layers will hinder the electron transmission between RGO layers, resulting in the decrease of fiber conductivity. So PEDOT:PSS content in PEDOT:PSS/RGO fiber should be limited to less than or equal to 20 wt%.

The tensile strength ($301.1 \pm 41.7 \text{ MPa}$) and elongation at break (5.4%) of PG3 fibers were 300% and 1.4 times larger than the tensile strength and elongation of RGO fibers, respectively. The $>5\%$ elongation of PG3 fiber indicates that RGO fibers showed excellent flexibility against fracture under tensile stress, which can promote their processability in the textile industry. The fracture toughness and improved strength of PG3 fibers may have been due to strong $\pi-\pi$ interactions of PEDOT with GO sheets, as shown by the FTIR spectrum in Figure 2. When the solid electrolyte was loaded on the fiber, the tensile

strength of PG3-Agl fibers further improved to 322.0 ± 17.0 MPa, possibly because Agl particles filled the fiber defects.

With high strength and excellent flexibility, the PEDOT-doped RGO fibers also obtained a high electrical conductivity (10^4 S m^{-1}), which is consistent with literature values for RGO fibers.^[45,46] The conductivity of PG3 fibers, which was produced from a spinning solution containing 20 wt% of PEDOT:PSS, was 161 S cm^{-1} . This was also attributed to the π - π stacking of PEDOT:PSS (Figure 2a) and interactions between PEDOT and RGO sheets demonstrated in the FTIR spectrum.

Electrochemical properties

PG3-Agl fiber, PG3 fiber, and RGO fiber were respectively assembled into symmetric supercapacitors with gel electrolyte of poly(vinyl alcohol)/sulfuric acid. Each electrode was composed of eight 1 cm long fibers using a two-electrode set-up to investigate its electrochemical properties (Figures 4 and S4).

At the high scan rate of 100 mV s^{-1} , the CV curves of RGO, PG3, and PG3-Agl FSCs maintained a quasi-rectangular shape (Figure 4a), which was close to ideal capacitance performance. The introduction of PEDOT:PSS in the RGO fiber improved the capacitive behavior of RGO FSC. While growing Agl on PG3 fiber, the capacitance of PG3-Agl FSC was prominently enlarged. The peak current density can reach to ~ 12 A cm^{-3} for the PG3-Agl FSC (Figure 4a). Notably, the potential window of PG3-Agl FSC reached 1.6 V (Figure 4a), which is remarkably higher than that of FSCs reported previously.^[45,47–55] The wide potential window and high specific capacitance of PG3-Agl

should be attributed to with micro and nano Agl particles on the RGO composite fibers. As we all know, Agl was the ionic conductor or semi-conductor. When was employed voltage, I⁻ was fixed in the lattice and Ag⁺ can move through defects whose ionic conductivity can reach 1 S/cm depending on the Agl micro structure.^[56,57] According to Equation (1), the volumetric capacitance of PG3-Agl FSC reached 203.1 F cm^{-3} at a scan rate of 5 mV s^{-1} , which is 3.3 and 2.1 times larger than that of RGO FSC (61.8 F cm^{-3}) and PG3 FSC (99.2 F cm^{-3}), respectively.

At 5 and 10 mV s^{-1} low scan rates, the CV curves of PG3-Agl FSCs displayed strong redox peaks of PEDOT (Figure 4c). At 50 and 100 mV s^{-1} high scan rates, the CV curves displayed quasi-rectangular shape. The volumetric capacitance of PG3-Agl, RGO and PG3 FSCs all exhibit decreasing when the FSC was scanned from 5 mV s^{-1} to 100 mV s^{-1} (Figure 4e). When the prepared FSCs was scanned at high rate, the charging and discharging process was too fast that active substances have no time to respond and migrate, so the capacity of the FSC showed a rapid reduction. For PG3-Agl FSC, due to the photosensitivity of Agl and its structure are mainly β phase and γ phase, as the test progresses, the role of Agl as ion conductivity is also failed.

In the GCD curves of the prepared FSCs, there were linear relationships between potentials and times (Figure 4b). There was no obvious *iR* drop in the curves, which indicated that the prepared FSCs had excellent charge-transfer performances. According to Equation (2), the specific capacitance of PG3-Agl is 166.6 F cm^{-3} , which is 2.3 times of RGO (71.1 F cm^{-3}) and 1.1 times of PG3 (160.8 F cm^{-3}), showing excellent capacitance performance. At different current densities in Figure 4(d), the

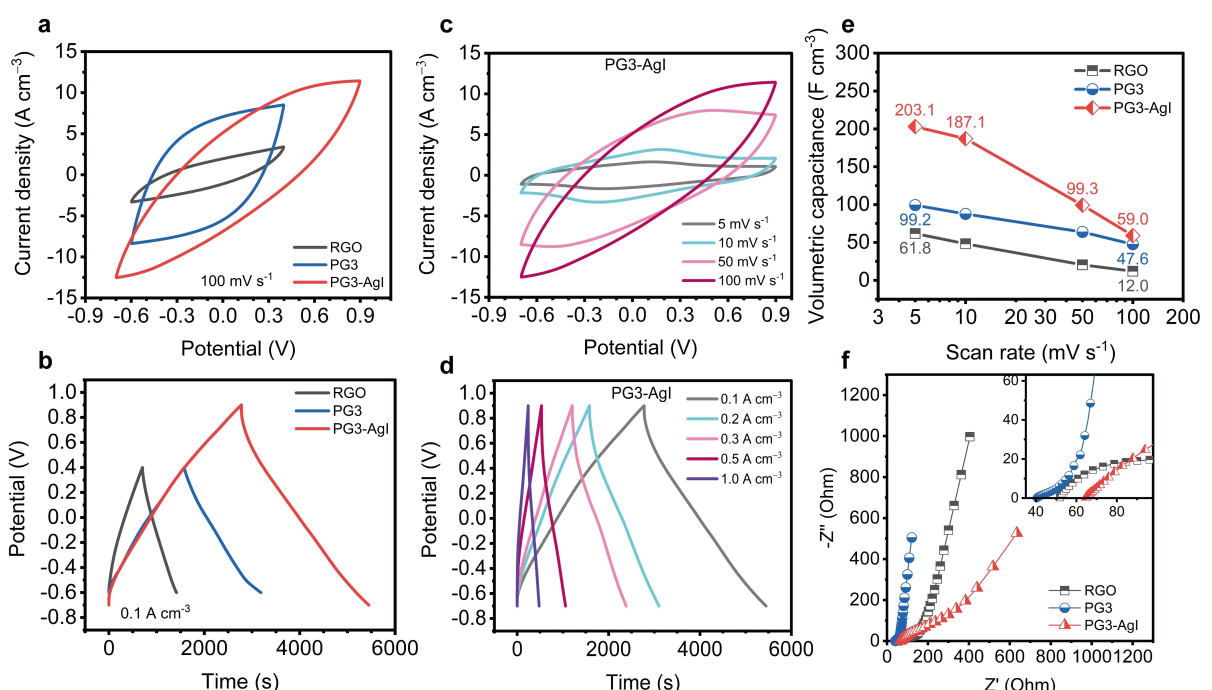


Figure 4. a) The cyclic voltammetry (CV) curves (obtained with different potential windows at a 100 mV s^{-1} scan rate) and b) galvanostatic charge-discharge (GCD) curves (obtained at a 0.1 A cm^{-3} current density) of RGO, PG3, and PG3-Agl FSCs. c) The CV and d) GCD curves of PG3-Agl FSCs. The CV and GCD curves were obtained at various scan rates and different current densities, respectively. e) The volumetric capacitance of PG3-Agl FSCs at different scan rate. f) Electrochemical impedance spectroscopy (EIS) curves of RGO, PG3, and PG3-Agl FSCs.

GCD curves maintained quasi isosceles triangles, which means charge-discharge efficiencies were close to 100%. The capacitance retention was 89% from 0.1 A cm⁻³ of 166.6 F cm⁻³ to 1.0 A cm⁻³ of 148.5 F cm⁻³.

In order to explore the mechanism of PG3-Agl ultra-high energy density, the EIS impedance curves of RGO, PG3 and PG3-Agl were displayed in Figure 4(f), which included high frequency semicircle (representing charge transfer) and low frequency straight line (representing matter transfer). EIS Equivalent circuit of RGO, PG3, and PG3-Agl FSCs was shown in Figure S5. The semicircle diameter was the charge transfer resistance (R_{ct}). Among RGO, PG3, and PG3-Agl FSCs, PG3 FSC shows lowest R_{ct} (3.6 Ω) compared with that of RGO (96.3 Ω) and of PG3-Agl (48.2 Ω), which may result from their different electronic conductivity. The linear slope of PG3 in the low frequency region is close to 90°, which is approach to the ideal capacitance behavior. The linear slope in low frequency region of PG3-Agl is close to 45° which was Warburg diffusion, indicating that the ion diffusion is a kind of linear diffusion dominated by semi-infinite plane.^[58] When applied voltage, Ag⁺ in Agl broke away from the lattice bondage and migrated through defects, providing capacitance through chemical adsorption and desorption on the electrode surface.^[59] The hydrogen bond and π-π stacking interaction between PEDOT and RGO activate the electrochemical activity of the non-functional group -C=C-site, which enables Ag⁺ to intercalate between RGO and PEDOT to achieve intercalation

pseudocapacitance,^[60] resulting in excellent electrochemical performance of PG3-Agl FSC.

Application of PG3-Agl Fiber for FSCs

Compared with the reported literature, PG3-Agl has excellent energy density (Figure 5a). At a 40.08 mW cm⁻³ power density, PG3-Agl FSCs displayed an ultrahigh volumetric energy density (E_v , 29.65 mWh cm⁻³) ascribed to the broad potential window. The E_v is higher than that of CNT/RGO composite fiber (3.4 mWh cm⁻³),^[61] RGO/cellulose nanocrystal fiber (5.1 mWh cm⁻³),^[62] RGO/PANI hybrid fiber (8.8 mWh cm⁻³),^[10] RGO/MXene hybrid fiber (5.1 mWh cm⁻³),^[63] MXene/PEDOT hybrid fiber (7.13 mWh cm⁻³),^[17] MXene-functionalized graphene sheet (13.0 mWh cm⁻³)^[64] supercapacitors that have been reported in literatures. At a 399.16 mW cm⁻³ power density, the energy density of PG3-Agl FSCs remained at 26.4 mWh cm⁻³, which can ensure rapid charging in applications.

PG3-Agl FSC maintained nearly 88% of its initial capacitance and nearly 100% coulombic efficiency after 5000 charge-discharge cycles, exhibiting its outstanding cycling stability (Figure 5b). Notably, when the PG3-Agl FSC was bent at bending radius of 11.9, 7.8, and 1.0 mm, it displayed almost identical charge-discharge behavior (Figure 5c). In short, PG3-Agl FSCs simultaneously provided a wide potential window

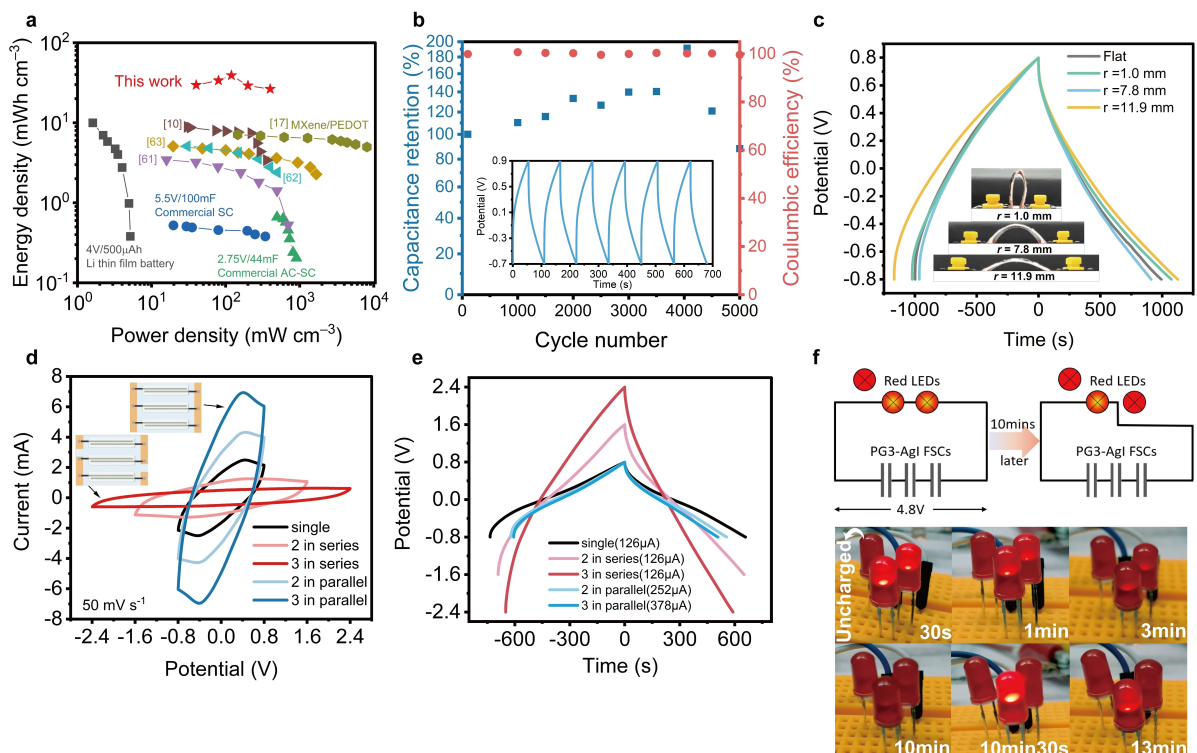


Figure 5. a) The Ragone plots of PG3-Agl FSCs and other reported supercapacitors. b) The capacitance retention performance through 5000 cycles GCD test of PG3-Agl FSCs. c) Bendability of PG3-Agl FSCs at different radius of curvature. d) The CV and e) GCD curves and schematic diagrams of multiple PG3-Agl FSCs connected in parallel or in series. f) Three PG3-Agl FSCs connected in series charged to 4.8 V can light two series-connected red LEDs for 10 min and then single red LED for 3 min.

(1.6 V), high electrical conductivity, excellent tensile strength, a high power density, and a high energy density. This provided advantages over other reported graphene composite FSCs (Table S1).^[65–70]

To verify PG3-Agl FSCs performance in wearable electronics at various voltage and/or power needs, multiple PG3-Agl FSCs were assembled in series or in parallel to increase current output or voltage output. The potential windows of two PG3-Agl FSCs assembled in series reached 3.2 V and 4.8 V for three (Figure 5d), which have been on-par with commercial organic lithium-ion film batteries. The voltage of the FSCs in series devices was positively correlated to the number of FSCs. The shapes of the CV curves of multiple FSCs connected in series were approximately rectangular, even at a relatively high scanning rate (50 mVs^{-1}). When 2 and 3 FSCs were connected in series or in parallel, the charging and discharging time of GCD tests were basically unchanged (Figure 5e), which indicates that a certain number of FSCs connected in series or in parallel could meet the need for achieving potential and current required for supplying external devices.

In demo application experiments, three in-series FSCs light two series-connected red LEDs (which totally requires $\sim 4 \text{ V}$) for 10 min, as shown in Figure 5(f). After 10 min, the remaining capacitance could still illuminate one red light LED for over 3 min. This shows the great energy storage potential of PG3-Agl FSCs applied to wearable devices.

Conclusion

In order to accelerate the practical application of graphene fiber supercapacitors, Agl and conductive polymer assisted co-enhancement strategy was proposed to prepare the high-performance graphene fiber-based supercapacitors (GFSCs) with superhigh energy density, favorable mechanical properties and superior electrochemical properties. Poly(3,4-ethylenedioxothiophene) (PEDOT) was used as a conductive binder to connect RGO flakes, and the PEDOT:PSS/RGO hybrid fibers show higher electrochemical performance and 300% higher tensile strength compared to the RGO fiber. Raman spectroscopy and Fourier transform infrared spectroscopy revealed synergistic $\pi-\pi$ stacking and hydrogen bonding interactions between PEDOT:PSS and GO sheets which made PEDOT tend to form a planar conformation that embedding in the RGO sheets and bonding the RGO sheet closely. Furthermore, Agl/PEDOT:PSS(20%)/RGO(80%) fibers (PG3-Agl) were obtained by depositing the solid electrolyte Agl on the surface of PG3 fibers using the hydroiodic acid from the reduction of RGO fibers. The tensile strength of the PG3-Agl fibers was 322 MPa. The potential window of PG3-Agl FSCs reached 1.6 V and specific volumetric capacitance attained 203.1 Fcm^{-3} at 5 mVs^{-1} , 166.6 Fcm^{-3} at 0.1 Acm^{-3} respectively. The best energy density and power density of the FSCs were 29.65 mWhcm^{-3} and 399.16 mWcm^{-3} , respectively. Due to their outstanding strength, elongation at break, and energy density, PG3-Agl fibers can be sewn into garments to power wearable electronics.

Experimental Methods

Synthesis of PEDOT:PSS: 3,4-Ethylenedioxothiophene (EDOT, $\geq 99.8 \text{ wt\%}$) was purchased from Suzhou Yake Chemical Reagent Co., Ltd. Poly(4-styrenesulfonic acid) (PSS, $M_n = 70\,000\text{--}80\,000$, 30 wt%) was obtained from Shanghai Xirun Chemical Industry Co., Ltd. A mixture obtained by adding EDOT and PSS (mol EDOT: mol PSS = 1:1) to deionized water was stirred for 20 min. Then, sodium persulfate (1 M) was added to this mixture under magnetic stirring for 15 min at $20\text{--}30^\circ\text{C}$. Finally, ferric chloride solution (0.3 M) was added to the above reaction system at the speed of 0.01 mL per second, and the mixture was stirred for 24 h. PEDOT:PSS aqueous solution was obtained by centrifugal washing three times.

Preparation of spinning formulation: Graphene oxide (GO) article was sonicated in deionized water for 2 h to obtain an 18 mg mL^{-1} GO solution. PEDOT:PSS and GO solutions were mixed and concentrated to prepare different formulations of PEDOT:PSS/GO spinning solutions.

Wet-spinning of PEDOT:PSS/RGO composite fibers: An 18-gauge blunt needle with a 0.84 mm inner diameter was attached to a 20 mL syringe (Becton Dickinson) into which a PEDOT:PSS/GO spinning solution was loaded. After the mounting of the syringe onto a syringe pump (LEADFLUID TYD01), the spinning solution was extruded into an acetic acid bath. The flow rate of the solution was 0.2 mL min^{-1} , and the extrudate was soaked for 15 min. Afterwards, acetic acid was replaced with 47 wt% hydroiodic acid, and the fibers were reduced at room temperature for 12 h. After that, the fibers were washed with ethanol three times, washed with deionized water three times, collected on a cylinder, and dried at room temperature to obtain PEDOT:PSS/RGO composite fibers. Fibers with PEDOT:PSS mass contents of 10%, 15%, 20%, 25%, 30%, 40%, and 50% were named PG1, PG2, PG3, PG4, PG5, PG6, and PG7, respectively.

Loading of solid electrolyte: After being reduced, the RGO composite fiber containing 20 wt% PEDOT:PSS without washing in water or ethanol was placed in 10 mg mL^{-1} silver nitrate/ethanol solution for 2 h to prepare PEDOT:PSS/RGO composite fiber loaded with solid electrolyte Agl. In this process, I^- adsorbed on fibers during RGO reduction was used to react with silver nitrate to produce a solid electrolyte that eliminated the washing step and environmental pollution. The fiber was collected on a cylinder, dried at room temperature, and named PG3-Agl.

Preparation of PVA/H₂SO₄ gel electrolyte: PVA and H₂SO₄ was applied to form gel electrolyte in fiber-shaped supercapacitor assembling (FSC). In short, PVA (1 g, $M_w = 75\,000$, Aladdin) and deionized water (10 mL) mixture were vigorously stirred at 85°C until a transparent solution was formed. The PVA solution was cooled to 25°C , and 1 g of H₂SO₄ (98 wt%) was added with stirring for 2 h. The PVA gel was vacuum-pumped for 12 h at room temperature.

Supercapacitor assembly: Eight composite fibers were twisted into one strand as a fiber electrode. Then, the two electrodes were arranged on the PET substrate to which copper foil was attached at both ends and bonded with conductive silver paste. After the silver paste dried, PVA/H₂SO₄ gel electrolyte was coated on and between two fiber electrodes to prepare a fiber-shaped supercapacitor (FSC).

Characterization and tests: The morphologies and elemental maps of RGO, PEDOT:PSS/RGO, and Agl/PEDOT:PSS/RGO fibers were characterized by a JEOL JSM-7500F scanning electron microscope (SEM) and an FEI QEMScan 650F SEM, respectively. XRD data were obtained from a Bruker D8 Advance X-ray diffractometer with Cu K α radiation ($\lambda = 1.54 \text{ \AA}$). The functional groups and molecular structures of the fibers were analyzed by a Bruker Tensor 27

Fourier-transform infrared spectrometer (FTIR) and a Horiba XploRA PLUS Raman spectrometer ($\lambda = 514$ nm), respectively. The electrical conductivity of the fibers was collected by a set of four-point probe facility (RTS-9 of Guangzhou Four Probe Technology Co., Ltd.), and 3 to 5 points were measured for each sample. INSTRON 5969 electronic universal material strength tester was used to record the stress and strain curves of the fibers, with a 20 mm clamping distance, extension rate of 5 mm min^{-1} , and 3 to 5 times for each sample testing.

The electrochemical performances of RGO, PG3, and PG3-Agl FSCs were characterized by a CS electrochemical workstation (Wuhan Coster Instrument Co., Ltd.) using a two-electrode setup. The cyclic voltammetry (CV) and galvanostatic charge-discharge (GCD) curves of PG3-Agl FSCs were measured at multiple scan rates (5, 10, 50, and 100 mVs^{-1}) and multiple current densities (0.1, 0.2, 0.3, 0.5, and 1.0 A cm^{-3}), respectively. The long-term cyclic stability of PG3-Agl FSCs was tested for 5000 cycles under a 0.5 A cm^{-3} current density.

For the all-solid two-electrode device, the current in the CV curve and current density in the GCD curve were calculated according to the volume of the PGx fiber electrode. The CV and GCD curves were used to calculate the volumetric capacitance ($C_v, \text{ F cm}^{-3}$) of the device according to Equation (1) and Equation (2), respectively.

$$C_d = \frac{\int I dU}{2v\Delta U} \quad (1)$$

$$C_d = \frac{it}{\Delta U - U_{IR}} \quad (2)$$

where $\int I dU$ is the integrated area of the closed CV curves, v is the voltage scan rate (Vs^{-1}), ΔU is the potential window (V), i is the discharge current (A), t is the discharge time (s), and U_{IR} is the voltage drop on the discharge curve.

Equation (3) was used to calculate the volumetric specific capacitance of the device ($C_{d,v}$):

$$C_{d,v} = \frac{C_d}{V_d} \quad (3)$$

where V_d is the volume of one electrode.

Equations (4) and (5) were used to calculate the energy density (E_v) and power density (P_v) of the device.

$$E_v = \frac{1}{2} C_{d,v} (\Delta U - U_{IR})^2 \quad (4)$$

$$P_v = \frac{E_v}{t} \quad (5)$$

Acknowledgements

This work was supported by the National Natural Science Foundation of China (52173001), the Special Fund for the Construction of High-level Teachers in Beijing Institute of Fashion Technology (BIFT2020002345), and the National Advanced Printing and Dyeing Technology Innovation Center (ZJ2021A06).

Conflict of Interest

The authors have no conflict of interest to declare.

Data Availability Statement

The data that support the findings of this study are available from the corresponding author on reasonable request.

Keywords: fiber-shaped supercapacitors • graphene fibers • PEDOT:PSS • solid electrolyte AgI

- [1] J. Subramanian In *Organic Transistors on Fiber: A First Step Toward Electronic Textiles*, INTERNATIONAL ELECTRON DEVICES MEETING, 2003.
- [2] H. H. Yong, Y. K. Chan, S. U. Kong, K. C. Choi, *SID International Symposium: Digest of Technology Papers* 2022, 53, 577.
- [3] Y. Wu, F. Guan, X. Li, Y. Gong, X. Wang, J. Zhou, Y. Chen, *Fibers Polym.* 2022, 23, 626.
- [4] B. Fang, D. Chang, Z. Xu, C. Gao, *Adv. Mater.* 2020, 32, 1902664.
- [5] L. Huang, D. Santiago, P. Loyselle, L. Dai, *Small* 2018, 14, 1800879.
- [6] W. Liu, M. S. Song, B. Kong, Y. Cui, *Adv. Mater.* 2017, 29, 1603436.
- [7] M. Lu, *Supercapacitors: materials, systems, and applications*, John Wiley & Sons, 2013.
- [8] D. Yu, S. Zhai, W. Jiang, K. Goh, L. Wei, X. Chen, R. Jiang, Y. Chen, *Adv. Mater.* 2015, 27, 4895.
- [9] N. Yu, H. Yin, W. Zhang, Y. Liu, Z. Tang, M.-Q. Zhu, *Adv. Energy Mater.* 2016, 6, 1501458.
- [10] P. Li, Z. Jin, L. Peng, F. Zhao, D. Xiao, Y. Jin, G. Yu, *Adv. Mater.* 2018, 30, 1800124.
- [11] W. Liu, K. Feng, Y. Zhang, T. Yu, L. Han, G. Lui, M. Li, G. Chiu, P. Fung, A. Yu, *Nano Energy* 2017, 34, 491.
- [12] K. Ren, Z. Liu, T. Wei, Z. Fan, *Nano-Micro Lett.* 2021, 13, 129.
- [13] N. Wang, X. Wang, Y. Zhang, W. Hou, Y. Chang, H. Song, Y. Zhao, G. Han, *J. Alloys Compd.* 2020, 835, 155299.
- [14] N. Choudhary, C. Li, J. Moore, N. Nagaiah, L. Zhai, Y. Jung, J. Thomas, *Adv. Mater.* 2017, 29, 1605336.
- [15] Q. Gou, S. Zhao, J. Wang, M. Li, J. Xue, *Nano-Micro Lett.* 2020, 12, 98.
- [16] Z. Pan, J. Yang, Q. Zhang, M. Liu, Y. Hu, Z. Kou, N. Liu, X. Yang, X. Ding, H. Chen, J. Li, K. Zhang, Y. Qiu, Q. Li, J. Wang, Y. Zhang, *Adv. Energy Mater.* 2019, 9, 1802753.
- [17] J. Zhang, S. Seyedin, S. Qin, Z. Wang, S. Moradi, F. Yang, P. A. Lynch, W. Yang, J. Liu, X. Wang, J. M. Razal, *Small* 2019, 15, 1804732.
- [18] G. Qu, J. Cheng, X. Li, D. Yuan, P. Chen, X. Chen, B. Wang, H. Peng, *Adv. Mater.* 2016, 28, 3646.
- [19] T. Zhou, Q. Cheng, *Angew. Chem., Int. Ed. Engl.* 2021, 60, 18397.
- [20] C. Liu, Z. Yu, D. Neff, A. Zhamu, B. Z. Jang, *Nano Lett.* 2010, 10, 4863.
- [21] X. Xia, J. Zhan, Y. Zhong, X. Wang, J. Tu, H. J. Fan, *Small* 2017, 13, 1602742.
- [22] X. Xia, Y. Zhang, D. Chao, Q. Xiong, Z. Fan, X. Tong, J. Tu, H. Zhang, H. J. Fan, *Energy Environ. Sci.* 2015, 8, 1559.
- [23] D. Yu, K. Goh, H. Wang, L. Wei, W. Jiang, Q. Zhang, L. Dai, Y. Chen, *Nat. Nanotechnol.* 2014, 9, 555.
- [24] X. He, Z. Tang, L. L. Gao, F. Wang, S. Zhuo, *J. Electroanal. Chem.* 2020, 871, 114311.
- [25] H. Jiang, D. Yuan, D. Huang, B. Lin, J. Li, P. Guo, Y. Wang, *Appl. Surf. Sci.* 2022, 585, 1526951.
- [26] Z. Wang, J. Cheng, J. Zhou, J. Zhang, H. Huang, J. Yang, Y. Li, B. Wang, *Nano Energy* 2018, 50, 106.
- [27] Q. Chen, F. Zabihi, M. Eslamian, *Synth. Met.* 2016, 222, 309.
- [28] S. Lin, J. Tang, K. Zhang, T. S. Suzuki, Q. Wei, M. Mukaida, Y. Zhang, H. Mamiya, X. Yu, L.-C. Qin, *J. Power Sources* 2021, 482, 228995.
- [29] B. B. Owens, *J. Power Sources* 2000, 90, 2.
- [30] M. Armand, J. M. Tarascon, *Nature* 2008, 451, 652.
- [31] S. Sarangapani, B. V. Tilak, C. P. Chen, *J. Electrochem. Soc.* 1996, 143, 3791.
- [32] R. Makiura, T. Yonemura, T. Yamada, M. Yamauchi, R. Ikeda, H. Kitagawa, K. Kato, M. Takata, *Nat. Mater.* 2009, 8, 476.

- [33] C. Liang, K. Terabe, T. Hasegawa, M. Aono, N. Iyi, *J. Appl. Phys.* **2007**, *102*, 415.
- [34] E.I. Biru, H. Iovu, *Graphene Nanocomposites Studied by Raman Spectroscopy*, IntechOpen, London, UK **2018**.
- [35] H. J. Lee, G. Anoop, H. J. Lee, C. Kim, J.-W. Park, J. Choi, H. Kim, Y.-J. Kim, E. Lee, S.-G. Lee, Y.-M. Kim, J.-H. Lee, J. Y. Jo, *Energy Environ. Sci.* **2016**, *9*, 2806.
- [36] D. Yoo, J. Kim, J. H. Kim, *Nano Res.* **2014**, *7*, 717.
- [37] K. Krishnamoorthy, M. Veerapandian, K. Yun, S.-J. Kim, *Carbon* **2013**, *53*, 38.
- [38] G. H. Kim, D. H. Hwang, S. I. Woo, *Phys. Chem. Chem. Phys.* **2012**, *14*, 3530.
- [39] J. Atoyo, M. R. Burton, J. McGettrick, M. J. Carnie, *Polymers* **2020**, *12*, 559.
- [40] J. Ouyang, Q. Xu, C.-W. Chu, Y. Yang, G. Li, J. Shinar, *Polymer* **2004**, *45*, 8443.
- [41] H. Yan, T. Ohta, N. Toshima, *Macromol. Mater. Eng.* **2001**, *286*, 139.
- [42] Q. Yao, L. Chen, X. Xu, C. Wang, *Chem. Lett.* **2005**, *34*, 522.
- [43] A. G. MacDiarmid, A. J. Epstein, *Synth. Met.* **1995**, *69*, 85.
- [44] M. A. Zahed, S. C. Barman, P. S. Das, M. Sharifuzzaman, H. S. Yoon, S. H. Yoon, J. Y. Park, *Biosens. Bioelectron.* **2020**, *160*, 112220.
- [45] B. Li, J. Cheng, Z. Wang, Y. Li, W. Ni, B. Wang, *J. Power Sources* **2018**, *376*, 117.
- [46] T. Xu, D. Yang, Z. Fan, X. Li, Y. Liu, C. Guo, M. Zhang, Z.-Z. Yu, *Carbon* **2019**, *152*, 134.
- [47] Y. Fu, X. Cai, H. Wu, Z. Lv, S. Hou, M. Peng, X. Yu, D. Zou, *Adv. Mater.* **2012**, *24*, 5713.
- [48] K. Guo, Y. Ma, H. Li, T. Zhai, *Small* **2016**, *12*, 1024.
- [49] L. Kou, T. Huang, B. Zheng, Y. Han, X. Zhao, K. Gopalsamy, H. Sun, C. Gao, *Nat. Commun.* **2014**, *5*, 3754.
- [50] A. Rafique, A. Massa, M. Fontana, S. Bianco, A. Chiodoni, C. F. Pirri, S. Hernández, A. Lamberti, *ACS Appl. Mater. Interfaces* **2017**, *9*, 28386.
- [51] J. Ren, W. Bai, G. Guan, Y. Zhang, H. Peng, *Adv. Mater.* **2013**, *25*, 5965.
- [52] F. Su, X. Lv, M. Miao, *Small* **2015**, *11*, 854.
- [53] B. Wang, Q. Wu, H. Sun, J. Zhang, J. Ren, Y. Luo, M. Wang, H. Peng, *J. Mater. Chem. A* **2017**, *5*, 925.
- [54] P. Xu, T. Gu, Z. Cao, B. Wei, J. Yu, F. Li, J.-H. Byun, W. Lu, Q. Li, T.-W. Chou, *Adv. Energy Mater.* **2014**, *4*, 1300759.
- [55] D. Yuan, B. Li, J. Cheng, Q. Guan, Z. Wang, W. Ni, C. Li, H. Liu, B. Wang, *J. Mater. Chem. A* **2016**, *4*, 11616.
- [56] G. Y. Li, *Solid State Ionics* **1988**, *28*, 1473.
- [57] J. Tallon, *Phys. Rev. B* **1987**, *36*, 776.
- [58] J. Song, M. Z. Bazant, *J. Electrochem. Soc.* **2013**, *160*, A15.
- [59] L. Wang, M. Peng, J. Chen, X. Tang, L. Li, T. Hu, K. Yuan, Y. Chen, *ACS Nano* **2022**, *16*, 2877.
- [60] Z. Hu, X. Zhao, Z. Li, S. Li, P. Sun, G. Wang, Q. Zhang, J. Liu, L. Zhang, *Adv. Mater.* **2021**, *33*, 2104039.
- [61] Y. Ma, P. Li, J. W. Sedloff, X. Zhang, H. Zhang, J. Liu, *ACS Nano* **2015**, *9*, 1352.
- [62] G. Chen, T. Chen, K. Hou, W. Ma, M. Tebyetekerwa, Y. Cheng, W. Weng, M. Zhu, *Carbon* **2018**, *127*, 218.
- [63] S. Seyedin, E. R. S. Yanza, Joselito M. Razal, *J. Mater. Chem. A* **2017**, *5*, 24076.
- [64] T. Zhou, C. Wu, Y. Wang, A. P. Tomsia, M. Li, E. Saiz, S. Fang, R. H. Baughman, L. Jiang, Q. Cheng, *Nat. Commun.* **2020**, *11*, 2077.
- [65] G. Xin, W. Zhu, Y. Deng, J. Cheng, L. T. Zhang, A. J. Chung, S. De, J. Lian, *Nat. Nanotechnol.* **2019**, *14*, 168.
- [66] H. Ni, F. Xu, A. P. Tomsia, E. Saiz, L. Jiang, Q. Cheng, *ACS Appl. Mater. Interfaces* **2017**, *9*, 24987.
- [67] Y. Cheng, J. Peng, H. Xu, Q. Cheng, *Adv. Funct. Mater.* **2018**, *28*, 1800924.
- [68] S. Wan, Y. Chen, Y. Wang, G. Li, G. Wang, L. Liu, J. Zhang, Y. Liu, Z. Xu, A. P. Tomsia, L. Jiang, Q. Cheng, *Matter* **2019**, *1*, 389.
- [69] W. Ma, W. Li, M. Li, Q. Mao, Z. Pan, M. Zhu, Y. Zhang, *J. Mater. Chem. A* **2020**, *8*, 25355.
- [70] W. Ma, W. Li, M. Li, Q. Mao, Z. Pan, J. Hu, X. Li, M. Zhu, Y. Zhang, *Adv. Funct. Mater.* **2021**, *31*, 2100195.

Manuscript received: December 12, 2022

Revised manuscript received: February 15, 2023

Accepted manuscript online: February 15, 2023

Version of record online: March 2, 2023